Evanescent-field Mach-Zehnder interferometer

Gagandeep Kaur [1,*] and Harshawardhan Wanare [1,2,†]
[1] *Centre for Lasers and Photonics, Indian Institute of Technology Kanpur, Kanpur, 208016, India*
[2] *Department of Physics, Indian Institute of Technology Kanpur, Kanpur, 208016, India*

(Received 13 October 2022; accepted 16 February 2023; published 16 March 2023)

We propose an evanescent-field interferometer in the Mach-Zehnder configuration, which can provide an interferometric measure of the phase of evanescent fields and can be used to quantify the Hartman effect. The phase difference for such tunneled fields saturates to $\pi/2$, thus confirming the classic Hartman effect. An analytical model of the proposed evanescent-field interferometer is presented and validated by numerical simulations based on the finite-difference time-domain technique. In the numerical treatment, the requisite elements of the interferometer, such as beam splitters and mirrors, are realized through carefully designed cavities in a two-dimensional photonic crystal system. The underlying cavity modes are further engineered using a weak perturbation to spatially maneuver the evanescent field along preferred directions. The evanescent-field interferometer offers multiple avenues of introducing phase delay and has higher sensitivity that is spatially delocalized in comparison to the conventional propagating-field interferometers.

DOI: 10.1103/PhysRevA.107.033506

I. INTRODUCTION

Interferometry has been the singular most powerful tool for sensitive and precision measurements in science. It has brought about a revolution in our world view—from the famous Michelson interferometer in search of ether in 1880s [1] to the discovery of gravitational waves in recent times [2]. There have been multiple adaptations of interferometers depending on the specific application, such as the Mach-Zehnder interferometer, with its spatially separate paths for sensitive measurement of imbalances between the paths [3], and the common-path Sagnac interferometer, which is a stable workhorse for gyroscopes [4]. Cold atoms, electrons, neutrons, electromagnetic fields, and Bose-Einstein condensates have all been subjected to interference in a variety of geometries of interferometers [5–9], thus pushing the limits of metrology and simultaneously providing a rich tapestry of counterintuitive phenomena that furthers our fundamental understanding of nature. The present scientific literature related to interferometers is largely limited to the interference of propagating fields whose dynamical phase evolves along competing paths of the interferometer [3,10–12]. The fields evolve along various paths and then are combined together to create an interferogram that can be analyzed to quantify the minute differences in the paths.

We propose here an evanescent-field interferometer (EFI), wherein the evanescent fields along different spatial paths are combined to create an interferogram. Unlike the dynamical phase associated with propagating fields, the phase of the evanescent field is rarely invoked, as evanescent fields do not propagate [13], thus apparently rendering this proposal implausible. However, even though the use of propagating field has dominated interferometry, there is no fundamental barrier that prevents evanescent fields from exhibiting interference. The evanescent field traditionally has been relegated to merely supporting the propagating modes in waveguides as they exponentially decay away from the waveguide core. However, their important characteristic of tunneling through the cladding regions is widely exploited to achieve desired evanescent coupling between waveguides [14,15]. A one-to-one correspondence between evanescent-field tunneling and quantum tunneling across a barrier is well established [16]. This intriguing feature of tunneling governs the functioning of the ubiquitous cubic beam splitter, wherein the frustrated total internal reflection effect is implemented at the cojoined bases of two prisms [17–19] to control the input-output coupling.

One of the most counterintuitive phenomena associated with tunneling is the Hartman effect [20–23]. We believe that the proposed EFI can provide a direct measurement mechanism for the Hartman effect with interferometric accuracy. In the context of tunneling, the notion of dwell time, or the time spent by the particle (or wave packet) within the barrier, is the most pertinent aspect that has been widely explored [24–27]. The exponential decay of the amplitude due to tunneling is the dominant accompanying attribute. This naturally leads to significant pulse-shape distortions and the associated limitations in the measurement of tunneling time. The EFI configuration that we propose alleviates this pulse-shape-distortion issue to a large degree, as we discuss below.

Among the many measurement schemes that have been utilized to date, almost all schemes suffer from a rather unfair comparison of a nearly undistorted reference pulse with the tunneled (signal) pulse that has suffered significant distortion (including exponential decay of the amplitude and a substantial phase change) [24,28,29]. Such measurements in conventional interferometers are compromised due to poor fringe visibility, arising from unequal amplitudes of the reference

*kgagan@iitk.ac.in
†hwanare@iitk.ac.in

and signal pulses. Few research groups have tried to remove this ambiguity in the measurement of tunneling time and provided better techniques for measurements [30,31]. In the proposed EFI, the central drawback related to extreme pulse distortion is effectively addressed, as both the paths (i.e., the reference arm and the signal arm) are accessed by the evanescent fields that combine to create the interferogram. Thus, both the fields suffer nearly identical pulse-shape and amplitude distortions; thereafter, creation of any excess barrier in one arm can be precisely quantified from the resulting interferogram. The proposed EFI provides a much improved arsenal for such studies, and it can be used for both continuous and pulsed measurements. The outline of the paper is as follows.

We first propose a generic quantum tunneling model of interferometers in the Mach-Zehnder configuration. The model allows us to obtain the conventional (propagating) field interferometer and the tunneling-dominant EFI as limiting cases. The analytical model is then numerically validated in the photonic crystal system employing the finite-difference time-domain (FDTD) technique using the software MEEP [32]. We describe the design of the proposed EFI detailing all the required components such as beam splitters and mirrors for the evanescent fields. We further couple the two output ports of the EFI to propagating waveguides to facilitate their measurement. Incorporating all these elements results in complementary outputs along the two ports of the interferometer that depend on the phase difference acquired along the two tunneling pathways.

Photonic crystals (PCs) offer the best platform for implementation of the EFI because of their intrinsic flexibility and the control they offer with regard to design. PCs have found practical implementations in optical communication systems [33–37] and have also been extensively utilized for tunneling measurements [24,26] as the dwell time for a photonic band-gap structure is found to be identical to the associated group delay.

We provide specific design details for the realization of an EFI in the Mach-Zehnder geometry implemented in a two-dimensional (2D) PC structure. We compare the EFI with the conventional propagating-field-based Mach-Zehnder interferometer, which again is engineered within a 2D PC structure to highlight the stark difference between the two. The proposed EFI incorporates localized modes whose spatial field distribution is engineered to maneuver their evanescent-field tunneling [38] through various barriers to finally interfere. This is quite unlike the conventional schemes in which interferometers in PCs have been realized with self-collimated beams [36,37] that propagate freely and interfere. The main challenge of this proposal has been the realization of the requisite mirror and beam-splitter functionalities for spatial control of the evanescent field. These are realized using defect states, wherein the underlying spatial mode profile is controlled through incorporation of an appropriate weak perturbation confined well within a single unit cell [38]. This allows controlled manipulation of the spatial structure of the bound states and thus their accompanying tunneling. A controlled variation of the tunneling barrier height is introduced by changing the optical depth at suitable lattice sites to mimic barrier height variation, whose effects are captured in the resulting interferogram.

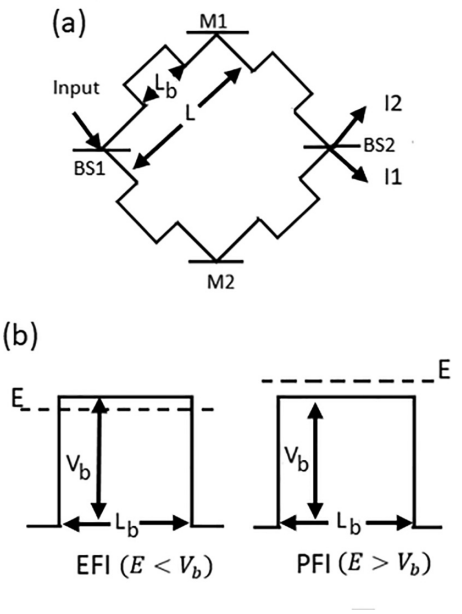

FIG. 1. Quantum tunneling-based Mach-Zehnder interferometer. (a) The interferometer design: BS1 and BS2 are 50:50 beam splitters, and M1 and M2 are mirrors. The total length of each path of the interferometer is $2L$, and the length of potential barrier is L_b, such that the length of free propagation in each path is $2(L - L_b)$. (b) Difference in two interferometers: The evanescent-field interferometer corresponds to $E < V_b$, whereas the conventional propagating-field interferometer has $E > V_b$.

II. ANALYTICAL MODEL

We consider a simplified quantum tunneling model which captures all the pertinent features of a generic Mach-Zehnder interferometer. We consider the basic Mach-Zehnder interferometer with two 50:50 beam splitters and two ideal reflecting mirrors [see Fig. 1(a)], wherein potential barriers are incorporated within the arms of the interferometer. The input after passing through the first beam splitter undergoes transmission through potential barriers as well as free propagation within each arm of the interferometer before reaching the second beam splitter, where the fields are combined together to create an interferogram. The energy of the input for the EFI is lower than the height of the potential barrier; thus, the particle experiences tunneling all through the arms of the interferometer. In contrast, the energy is considered to be higher than the barrier height for the propagating-field interferometer (PFI), as illustrated in Fig. 1(b). This is the central distinguishing feature that significantly separates the two interferometers. Except for input energy and barrier height, other parameters such as barrier width and the length of the arms of the interferometer are kept the same for both interferometers for ease of comparison.

The field through one arm of the interferometer (see Fig. 2) results in the following output:

$$\text{output field (at } x = L) = t_b e^{ikL}, \tag{1}$$

and the phase accumulated along the path

$$\phi = \phi_t + kL, \tag{2}$$

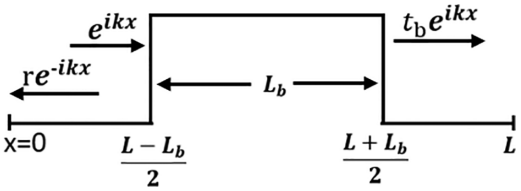

FIG. 2. Arm of the interferometer. Each arm consists of free propagation $(L - L_b)$ and a section with tunneling or propagation across a potential barrier of length (L_b).

where $\phi_t = \tan^{-1}(\frac{\mathrm{Im}(t_b)}{\mathrm{Re}(t_b)})$. We similarly construct the amplitude and phase along the two arms and combine them to obtain the intensities I_1 and I_2 at the two output ports. The output intensities for interferometers are given as

$$I_1 = \left|r_{s1}t_b e^{ikL} r_{m1} t_b e^{ikL} t_{s2} + t_{s1} t_b' e^{ikL} r_{m2} t_b e^{ikL} r_{s2}\right|^2 I_0, \quad (3)$$

$$I_2 = \left|r_{s1}t_b e^{ikL} r_{m1} t_b e^{ikL} r_{s2} + t_{s1} t_b' e^{ikL} r_{m2} t_b e^{ikL} t_{s2}\right|^2 I_0. \quad (4)$$

All the reflection and transmission amplitudes are described and tabulated in Table I. In order to capture the interferometric measure of the tunneling barrier, the barriers along one path are fixed, and one of the barriers in the other path is varied. All other parameters that govern the quantum tunneling interferometer model that are used for intensity and phase calculations of the interferometric output are included in Table I. The parameters of one of the potential barriers are varied in order to create a phase difference between the two interfering arms. In the analytical model, we consider two different cases, case A, in which the potential height V_b' of the barrier is changed, and case B, in which we change the barrier width L_b' for both interferometers. The following expressions provide the transmission amplitudes and phase for the EFI across the fixed and variable arms of the interferometer. The transmission amplitude for the fixed barrier is

$$t_b = \frac{e^{-ikL_b}}{\cosh(k_b L_b) + i\sinh(k_b L_b)\left(\frac{k_b}{2k} - \frac{k}{2k_b}\right)}, \quad (5)$$

the transmission amplitude for the varying barrier is

$$t_b' = \frac{e^{-ikL_b'}}{\cosh(k_b' L_b') + i\sinh(k_b' L_b')\left(\frac{k_b'}{2k} - \frac{k}{2k_b'}\right)}, \quad (6)$$

and

$$\phi_t = -kL_b - \tan^{-1}\left[\left(\frac{k_b}{2k} - \frac{k}{2k_b}\right)\tanh(k_b L_b)\right]. \quad (7)$$

Similarly, the transmission amplitudes and phase for PFI are as follows: The transmission amplitude for the fixed barrier is

$$t_b = \frac{e^{-ikL_b}}{\cos(k_b L_b) - i\sin(k_b L_b)\left(\frac{k_b}{2k} + \frac{k}{2k_b}\right)}, \quad (8)$$

and the transmission amplitude for the varying barrier is

$$t_b' = \frac{e^{-ikL_b'}}{\cos(k_b' L_b') - i\sin(k_b' L_b')\left(\frac{k_b'}{2k} + \frac{k}{2k_b'}\right)}, \quad (9)$$

with

$$\phi_t = -kL_b + \tan^{-1}\left[\left(\frac{k_b}{2k} + \frac{k}{2k_b}\right)\tan(k_b L_b)\right]. \quad (10)$$

Equations (5)–(10) are obtained by solving the Schrödinger equation with appropriately imposed boundary conditions. The propagation constants used in the above equations are

TABLE I. Values of parameters used in the quantum tunneling interferometer model. Case A corresponds to barrier-height variation, and case B corresponds to barrier-width variation.

Quantity	Symbol	Value	Remarks
Reflection amplitude at BS1	r_{s1}	$1/\sqrt{2}$	50:50 BS, phases in accordance with Ref. [38]
Transmission amplitude at BS1	t_{s1}	$-1/\sqrt{2}$	
Reflection amplitude at BS2	r_{s2}	$(i-1)/2$	
Transmission amplitude at BS2	t_{s2}	$-(i+1)/2$	
Reflection amplitude at M1	r_{m1}	1	
Reflection amplitude at M2	r_{m2}	1	
Propagation constant for free particle	k	$\sqrt{2mE/\hbar^2}$	Analytical model
Propagation constant in the fixed barrier, EFI	k_b	$\sqrt{2m(V_b - E)/\hbar^2}$	$E < V_b(V_b')$ for EFI
Propagation constant in the varying barrier, EFI	k_b'	$\sqrt{2m(V_b' - E)/\hbar^2}$	
Propagation constant in the fixed barrier, PFI	k_b	$\sqrt{2m(E - V_b)/\hbar^2}$	$E > V_b(V_b')$ for PFI
Propagation constant in the varying barrier, PFI	k_b'	$\sqrt{2m(E - V_b')/\hbar^2}$	
Case A			
Height of fixed barrier, EFI	V_b	1.51 (meV)	$E < V_b$ for EFI
Input energy, EFI	E	1.5 (meV)	
Height of fixed barrier, PFI	V_b	0.1 (meV)	$E \gg V_b$ for PFI as in real experiments
Input energy, PFI	E	180 (meV)	
Case B			
Height of fixed barrier, EFI and PFI	V_b	1 (meV)	$V_b - E$ (EFI) is equal to $E - V_b$ (PFI)
Input energy, EFI	E	0.98 (meV)	
Input energy, PFI	E	1.02 (meV)	

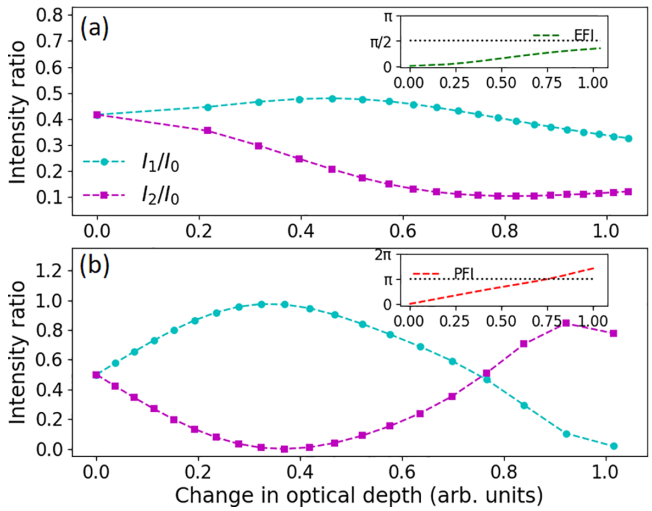

FIG. 3. Case A: Intensity variation versus change in optical depth. (a) Intensity observed for the evanescent-field interferometer with variation of the barrier height. (b) Intensity observed for the propagating-field interferometer with varying barrier height. The intensity ratio represents I_i/I_0, where $i = 1, 2$. I_1 and I_2 are the output intensities of the interferometer, and I_0 is the input intensity. The change in optical depth has units of length squared, with units of length being arbitrary. Inset: The accumulated phase difference (in radians) is shown as the optical depth is changed; note that the phase saturates at $\pi/2$ for the EFI.

included in Table I. For EFI, $E < V_b$, and $V_b' \geqslant V_b$; in contrast, for the conventional PFI we have $E > V_b'$ and $V_b' \geqslant V_b$, where V_b and V_b' are the heights of the fixed and varying barrier potentials along the two arms of the interferometer, respectively.

The optical depth equivalent to the one obtained in the PC implementation is $(\sqrt{|E - V_b|/V_b})L_b/k$. We plot the outputs I_1 and I_2 as a function of the difference in the optical depth along the two arms $\delta d = (\sqrt{|E - V_b'|/V_b})L_b'/k - (\sqrt{|E - V_b|/V_b})L_b/k$ for both interferometers (see Fig. 3). It is observed that for the EFI, on increasing the height of the potential barrier, the detector intensities vary slowly with the change in optical depth [see Fig. 3(a)] and saturate, whereas for PFI the detector intensities oscillate with the variation in optical depth, as observed in Fig. 3(b). For the same changes in optical depth the phase difference in the two arms of the interferometer for PFI goes beyond π, whereas for EFI the change in phase difference is gradual and tends to saturate close to $\pi/2$ (see Fig. 3), which clearly depicts the Hartman effect.

It may be noted that when the barrier width is changed while keeping the total arm length fixed, the free-space propagation itself varies in the arm and remains uncompensated. As a result, for EFI we see intensity oscillations in Fig. 4(a), and no phase saturation is seen due to the dominance of the uncompensated dynamical phase in one arm. In order to observe phase saturation in EFI, we need to ensure that the free-space length in both arms is balanced [see Fig. 4(b)]. It may be noted that in EFI for the cases where phase saturation is observed, the overall phase difference between two paths is given by

$$\delta\phi = -\tan^{-1}\left[\left(\frac{k_b}{2k} - \frac{k}{2k_b}\right)\tanh(k_b L_b)\right] + \tan^{-1}\left[\left(\frac{k_b'}{2k} - \frac{k}{2k_b'}\right)\tanh(k_b' L_b')\right]. \quad (11)$$

For both cases of phase saturation (i.e., with barrier height changed and with the change in the barrier width keeping the free-space length balanced), the second term in Eq. (11) tends to saturate and reach $\pi/2$ on changing barrier parameters, and it is the first term arising from the fixed barrier which decides to what value $\delta\phi$ saturates.

In the EFI, in order to have higher output intensities and better visibility, $|E - V_b|$ should be small, and barrier width should also be small in order to have sufficient transmission through the barrier. On the other hand, for PFI, larger $|E - V_b|$ leads to better visibility. We present the intensity and

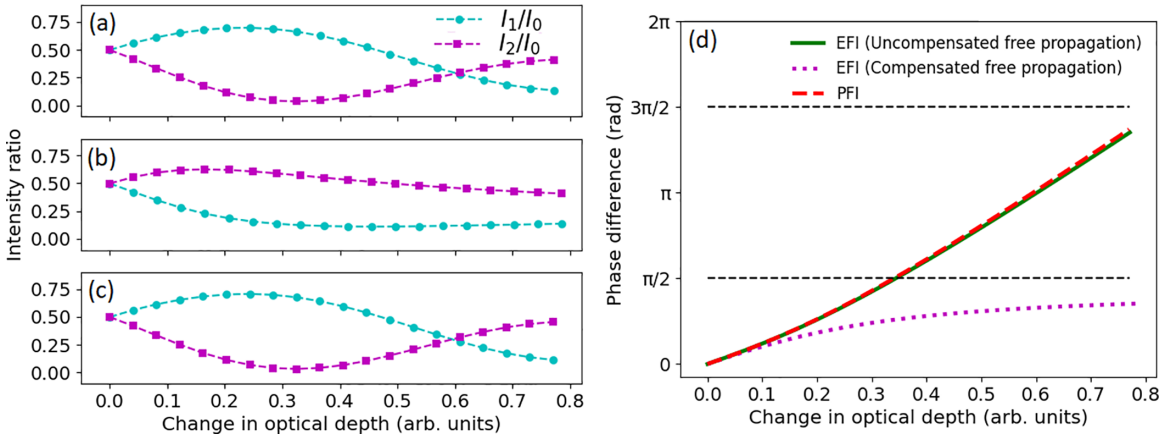

FIG. 4. Case B: Intensity variation versus change in optical depth and the corresponding phase difference. (a) EFI with barrier width changed while keeping the length of the arm fixed, which effectively results in a change in free propagation (uncompensated free propagation). (b) EFI with both the barrier width and arm length changed such that the free-propagation length remains fixed (compensated free propagation) and (c) PFI with uncompensated free propagation. The intensity ratio represents I_i/I_0, where $i = 1, 2$. I_1 and I_2 are the output intensities of the interferometer, and I_0 is the input intensity. (d) Phase difference accumulated between the two paths. The change in optical depth has units of length squared, with units of length being arbitrary.

phase-difference variation with the change in barrier width for both the interferometers (see Fig. 4). For lower values of the optical-depth change, both EFI and PFI show similar variations in terms of phase and intensity [see Figs. 4(a) and 4(c)]; however, at higher change in optical depth, the intensity continues to oscillate for PFI due to unbound phase accumulation, whereas for EFI the oscillations die out due to significantly reduced amplitudes beyond the barriers. It may also be noted that on changing the optical depth in the case of EFI, output intensities tend to saturate [see Fig. 4(b)]; however, if we continue to increase the barrier height, one arm will be completely shut off, and the remaining 50% of the field is equally divided at the second beam splitter, giving rise to a 25% output at each detector. Thus, we compare the two interferometers well below that range wherein a barrier in one arm completely blocks the field.

III. NUMERICAL DEMONSTRATION OF EFI IN PHOTONIC CRYSTAL STRUCTURE

In the previous section, we changed the optical depth along the arms of the interferometer using two methods, i.e., by changing the barrier height and barrier width. We compared both interferometers with these two changes and observed that for EFI the detector intensities and phase difference saturate, depicting the Hartman effect, whereas for PFI the detector intensities oscillate and phase difference increases in an unbounded manner. Now, we numerically validate these results seen for both interferometers by changing one of the parameters of the barrier, i.e., the dielectric constant or refractive index of the lattice rod, which is the equivalent of varying the barrier height.

A. EFI design with optical elements

We consider a system of a 2D PC with dielectric rods of radius $r = 0.2a$ and $\epsilon = 12$ arranged on a square lattice with a periodicity of a, resulting in a complete band gap for the TM polarization. In order to realize the mirrors and beam splitter for the evanescent field, we first create a defect that localizes the field akin to an optical cavity. The cavity modes are further engineered by weakly breaking the symmetry that alters the evanescent fields beyond the cavity, and we use this design tool to realize beam splitters and mirrors for the evanescent fields. The radius of the main defect rod for creating a cavity is $r_d = 0.33a$, such that there are doubly degenerate dipole resonant bound cavity modes. We add a much weaker perturbation rod with a size as small as $r_p \sim 0.05a$ close to the main defect rod, which lifts the degeneracy of the bound defect modes and spatially realigns the defect modes [38] along the direction of the added weak perturbation. It may be noted that the refractive index of the perturbation rod is higher than the lattice rods; however, the optical depth of the perturbation ($d = \pi r^2 \sqrt{\epsilon}$) is still much lower than that of rods which form the main lattice. Incorporation of a single perturbation rod at any angular position within the cavity can thus act as both a beam splitter and a mirror for the evanescent fields, depending upon its location within the structure, as illustrated in Fig. 5(a).

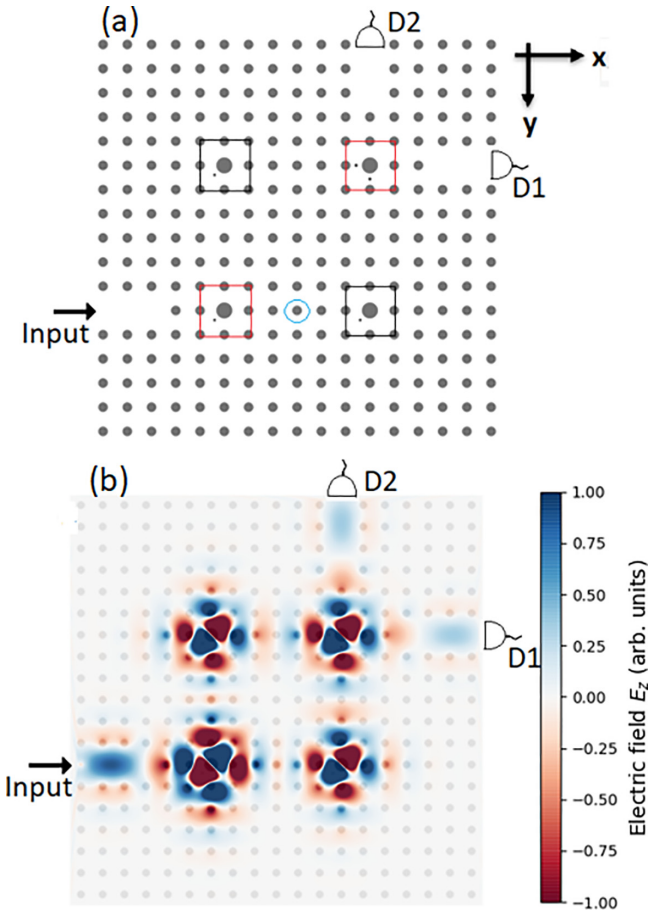

FIG. 5. Evanescent-field (Mach-Zehnder) interferometer. (a) A series of cavities are realized using a central defect rod with the modes engineered to align along the weak-perturbation rod. These tailored cavities act as beam splitters and mirrors highlighted within the red and black boxes, respectively. The optical depth of the rod circled in blue is varied to change the tunnel barrier along one arm of the interferometer. (b) Evanescent-field modes are supported along the two arms of the interferometer. The input and output (to D1 and D2) waveguides support propagating modes.

We first describe a 50:50 beam splitter that is incorporated along the input waveguide. After incorporation of the main cavity, a perturbation rod is added at an angular position of 135° with respect to the x axis to realize a beam splitter. Such a perturbation weakly breaks the symmetry and lifts the degeneracy of the dipole modes. For convenience we focus on only the lower-frequency mode in our analysis. The perturbation rods with similar angular orientations placed at the two opposite corners of interferometer [see Fig. 5(a)] make up the two mirror equivalents that channel the evanescent fields towards the output beam splitter. The second 50:50 (output) beam splitter is placed close to the output port waveguides. This output beam splitter consists of the main defect rod with two additional perturbation rods. The orientation of the perturbation rods is such that the resultant resonant dipole modes continue to be aligned along the 135° angular position; however, these modes are now designed to be degenerate. The evanescent fields along the two arms independently excite these (appropriately aligned) degenerate modes. This

degeneracy is critical to the working of the interferometer. It may be noted that the parameters of these two perturbation rods need to be carefully varied in order to obtain the same resonance frequency at each cavity comprising the mirrors and the beam splitters. Hence, in terms of the modal structure, all the resonant modes are oriented along 135° at every optical element, as is evident from the mode propagation profile in Fig. 5(b). Note the critical role of the perturbation rods that align the cavity modes to equally and preferentially direct the associated spatial distribution of the evanescent fields along the arms of the interferometer.

B. Operation of the EFI

When the input signal reaches the first beam splitter, the resonant mode is excited and decays equally along the arms of the interferometer and excites the mirror cavity modes. The spatial orientation of the modes is crucial in determining the associated evanescent field's direction of decay. The projection of the field being equal along the two paths results in decay-mediated coupling to the mirrors. This in turn excites the resonant modes at the respective mirror locations, which further decay along both the x and y axes. Finally, the doubly degenerate modes of the second beam splitter are excited independently by the incoming evanescent fields from both arms of the interferometer, and these modes interfere to provide the complementary outputs at detector 1 (D1) and detector 2 (D2) placed at port 1 and port 2, respectively. It should be noted that the doubly degenerate mode excitation actually creates a superposition of the respective modes [38] and the requisite phase difference that results in complementary output at D1 and D2. The phase difference between the modes is governed by the interfering fields exciting them. This can thus be controlled by introducing a change in the optical depth of lattice rods along the path, which is equivalent to changing the parameters of the potential barrier placed in the arms of interferometer as described in Sec. II. The important point to consider here is that the phases acquired in the path of the interferometer are not dynamical since the resonant modes tunnel through the arms to reach the second beam splitter. Hence, it is the phase linked to decaying evanescent fields that is being modulated, which is captured in the interferogram.

An increase in the refractive index of the dielectric rod [circled in Fig. 5(a)] results in a positive change in the optical depth; the output (energy density) at D1 increases, whereas the output at D2 decreases [see Fig. 6(a)]. Similarly, a negative change in optical depth is obtained by lowering the refractive index of the rod, and we obtain the opposite trend, as observed in Fig. 6(a). A higher change in optical depth along the paths starts to shift the resonance peaks (sharp resonances for EFI) of the defect modes along the path where the change is introduced. However, there is sufficient spectral overlap between two evanescent fields, resulting in significant interference. However, this shift in resonances may lead to poor evanescent coupling, thereby leading to reduced output.

We present another set of intensity and energy-density calculations targeting the higher-sensitivity rod location in Fig. 6(b). For the less sensitive rod location, the accumulated phase difference does not provide a high-visibility interferogram as we vary the optical depth involving positive and

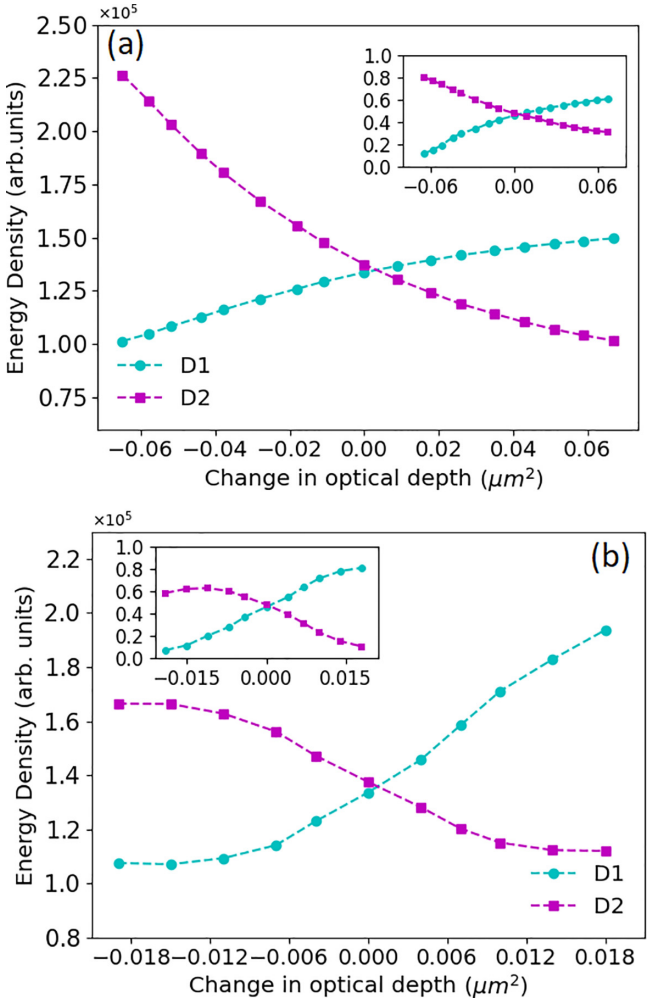

FIG. 6. Energy-density variation at the detectors versus the change (increase as well as decrease) in the optical depth of the dielectric rod in one arm of the evanescent-field interferometer. (a) The optical depth of the dielectric rod is varied at the lower-sensitivity location. (b) The optical depth of the dielectric rod at the high-sensitivity location is varied. D1 and D2 represent the complementary outputs at detector 1 and detector 2, respectively. The change in optical depth has units of length squared. Length is scaled according to the length of the unit cell; here it is taken as 1 μm. Inset: Intensity variation at the central frequency of interest at the two detectors; the visibility is obtained from such intensity levels.

negative changes in it. However, for the more sensitive rod locations both changes in optical depth result in comparable visibility close to 80%. The freedom to increase and decrease the optical depth is another approach to obtain better visibility, wherein optical depth can simultaneously be increased along one path and decreased along the other. Regarding the detection process, it may be noted that we present the visibility of the fringes from the intensity at the detectors. The intensity is calculated at the central frequency of interest. However, tracking the electromagnetic energy density also provides similar dependences (see Fig. 6). Furthermore, we have used the energy density as a true measure of the detected signal as it corresponds to the energy deposited in ideal index-matched detectors placed at D1 and D2 [39].

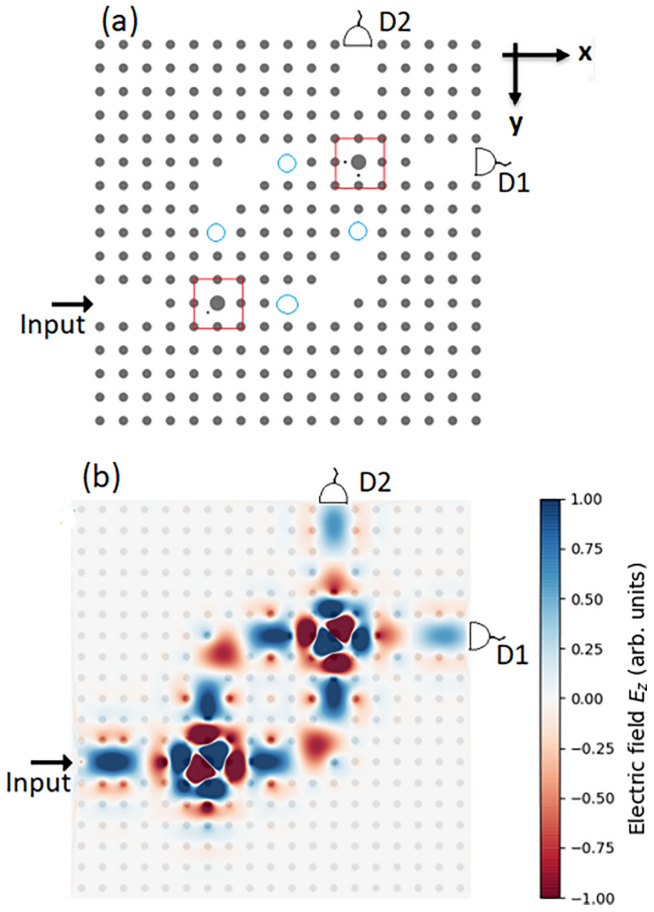

FIG. 7. The conventional propagating-field (Mach-Zehnder) interferometer. (a) The main defect rod with the perturbation rod continues to act as the beam splitter (highlighted within the red box), and the waveguide bends direct the field along the two arms of the interferometer, which combine again at the second beam splitter to form an interferogram. Dielectric rods with very low refractive index are introduced at the locations marked in blue circle, and the refractive index of these rods in one of the paths is varied to change the path length along that path of the interferometer. (b) Mode propagation profile for the PFI.

IV. COMPARISON OF EFI WITH CONVENTIONAL PFI

We briefly compare the conventional propagating-field Mach-Zehnder interferometer realized in a 2D PC structure with the evanescent-field interferometer. In PFI, dielectric rods are removed along the arms of the interferometer to create a waveguide and thereby eliminate the tunneling phenomena. Here the beam splitters remain the same as those of the EFI; however, no mirrors need to be incorporated as the photonic structure itself guides the propagating fields along the two paths. It is the band gap of photonic crystal that is utilized to obtain a controlled flow of light along desired pathways (see Fig. 7). The input signal is split by the first beam splitter, and the propagating fields pass through the two separate paths, finally reaching the second beam splitter and exciting the doubly degenerate modes independently, which interfere and provide complementary outputs at detectors D1 and D2, as seen in Fig. 8(b). It may be noted that in order to

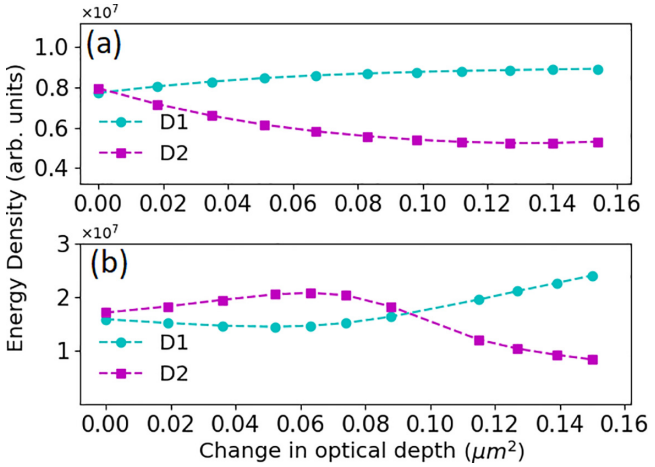

FIG. 8. Energy-density variation versus change in optical depth. (a) The interferogram obtained in the evanescent-field interferometer exhibits saturation of energy density at D1 and D2. (b) The propagating-field interferometer exhibits the usual oscillatory outputs at D1 and D2 as the optical depth along the arms is varied. D1 and D2 represent the complementary outputs at detector 1 and detector 2, respectively. The change in optical depth has units of length squared. Length is scaled according to the length of the unit cell; here it is taken as 1 μm.

create the same change in optical depth as for EFI, we add dielectric rods of very low refractive index in the middle of each arm, as marked in Fig. 7, and then increase the refractive index of these rods in one path to create a phase difference between interfering arms. We present in Fig. 8 a comparison of outputs at two detectors for EFI and PFI, corresponding to the same change in the optical depth.

A. Sensitivity of interferometers

The visibility of the interferogram at D1 and D2 obtained from intensity calculations depends on the spatial location and optical-depth change in the barrier lattice rods. Given the intrinsic exponential spatial dependence of the evanescent field, it is expected that the sensitivity to changes is spatially nonuniform, very unlike the conventional propagation-field interferometer where changes in optical depth remain uniformly sensitive only along the interferometer arms. The sensitivity of the interferometer is defined as the ratio of the change in detector intensity to the change in optical depth and is calculated for numerous rod locations spread over a large area of cross section (see Fig. 9). It is evident that the sensitivity of the EFI is not localized along the interfering paths like in the conventional propagating-field interferometers. It is observed that the interferometer is highly sensitive for rod locations close to resonant cavities [see Fig. 9(a)]; in fact, in the immediate neighborhood of the cavity, the sensitivity increases by a factor of 10 at each rod location as we move towards the cavity.

There is a striking difference between the sensitivities of the two interferometers as observed in Fig. 9. The sensitivity of locations within the arms of the interferometer changes quite drastically in the EFI and is spatially delocalized, whereas for the PFI this change is rather uniform along

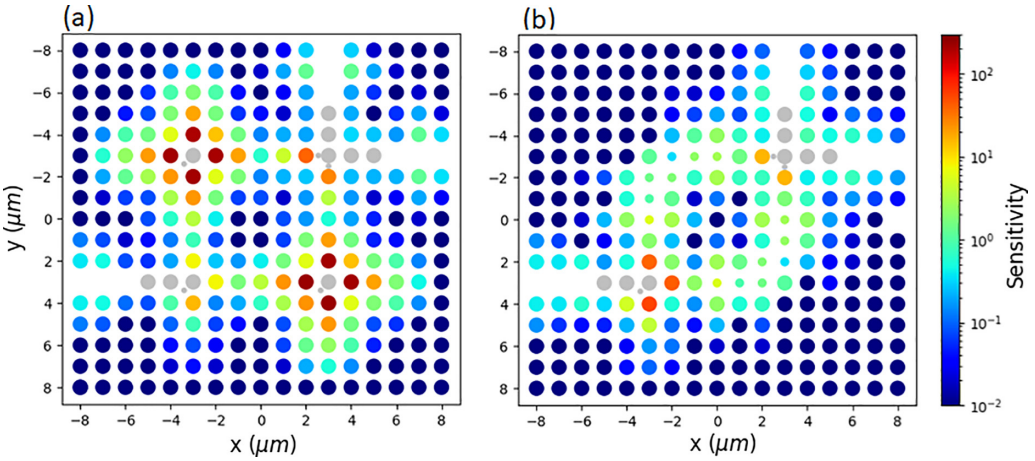

FIG. 9. Sensitivity plot for interferometers. (a) The evanescent-field interferometer has higher sensitivity which is spatially delocalized, and the exponential characteristics of the evanescent fields are captured in the sensitivity plots. (b) The propagating-field interferometer sensitivity is lower and largely uniform across the arms of the interferometer.

the two arms. As expected, the rods lying within the arms of the PFI are sensitive to changes in the optical depth, and the sensitivity decreases rapidly as one moves away from the interferometric arms. In contrast, for the EFI even the rods away from the arms (paths) of the interferometer are quite sensitive. The localized field within the cavities decays in all directions; hence, any change in optical depth in close proximity to the cavities significantly alters the output at the detectors. However, for the PFI it is the propagating field guided along the waveguide arms which interferes, and hence, any change in optical depth away from the waveguide arms does not affect the detector intensities. In terms of the absolute values of sensitivities too, the EFI has sensitivity larger by an order of magnitude ($\sim 10^1$) in comparison to the conventional PFI.

B. Hartman effect

The central result of the paper is the proposal for measurement of the phase difference arising purely out of variations in tunneling strength using the EFI. The energy densities tend to saturate even as the optical depth in the barrier region is increased [see Fig. 8(a)], which is a clear signature of the Hartman effect. On the other hand, for the PFI, Fig. 8(b) shows that the outputs vary continuously with the change in the optical depth in one arm. It can be inferred that for the EFI, the phase difference between the two interfering fields begins from zero and saturates to $\pi/2$ as the detector outputs saturate. However, in the conventional PFI, for the same change in the optical depth the phase difference goes beyond π and seems to be increasing continuously ($\pi \to 2\pi \to 3\pi \to \cdots$) with increasing optical depth. Altering the optical depth directly corresponds to a change in the potential barrier along the path of the interferometer, thereby leading to changes in tunneling time through the barrier. These phase changes and saturation validate the results obtained from the analytical model presented earlier. This saturation of phase, which is the signature of the Hartman effect, needs to arise purely due to changes in the tunnel barrier region, as already discussed in detail in Sec. II.

The photonic crystal implementation of the EFI presented here allows for pure variation of the tunneling barrier height and the resulting phase change captured through an interferometric protocol. It can most certainly be realized experimentally, and we envisage multiple dynamic ways of controlling the barrier height, either by focusing a laser beam onto a specific spatial spot along one of the interferometric arms within the path [12], thus inducing a refractive index change through the Kerr effect [40], or through electro-optic variation of the refractive index. The experimental challenge would arise from the detector noise at such low light levels.

V. CONCLUSION

In conclusion, we have proposed an evanescent-field interferometer in the Mach-Zehnder configuration, which was demonstrated analytically through a simple quantum tunneling model as well as implemented in a photonic crystal structure numerically with full-wave FDTD simulations. The design exploits the band gap of the photonic crystals to create tunneling barriers and implements mirror and beam-splitter cavities for the evanescent fields. The respective cavity modes are controlled further by weak perturbations that allow spatial mode rotation that steers the evanescent field along the arms of the interferometer. A detailed comparison with the conventional propagating-field interferometer established the unique phase saturation in the EFI resulting from tunneling. Thus, the proposed EFI provides clear evidence of the Hartman effect, and we believe that this can verify the Hartman effect with interferometric accuracy. Furthermore, the EFI exhibits enhanced as well as spatially delocalized sensitivity and can be utilized for various chemical and biosensing applications.

[1] A. A. Michelson, The relative motion of the earth and the luminiferous ether, Am. J. Sci. **s3-22**, 120 (1881).

[2] S. Vitale, The first 5 years of gravitational-wave astrophysics, Science **372**, eabc7397 (2021).

[3] M. Born and E. Wolf, *Principles of Optics: Electromagnetic Theory of Propagation, Interference and Diffraction of Light*, 7th ed. (Cambridge University Press, Cambridge, 2007).

[4] E. J. Post, Sagnac effect, Rev. Mod. Phys. **39**, 475 (1967).

[5] Y. Ji, Y. Chung, D. Sprinzak, M. Heiblum, D. Mahalu, and H. Shtrikman, An electronic Mach–Zehnder interferometer, Nature (London) **422**, 415 (2003).

[6] Y. Shin, M. Saba, T. A. Pasquini, W. Ketterle, D. E. Pritchard, and A. E. Leanhardt, Atom Interferometry with Bose-Einstein Condensates in a Double-Well Potential, Phys. Rev. Lett. **92**, 050405 (2004).

[7] T. Berrada, S. van Frank, R. Bücker, T. Schumm, J.-F. Schaff, and J. Schmiedmayer, Integrated Mach–Zehnder interferometer for Bose–Einstein condensates, Nat. Commun. **4**, 2077 (2013).

[8] A. D. Cronin, J. Schmiedmayer, and D. E. Pritchard, Optics and interferometry with atoms and molecules, Rev. Mod. Phys. **81**, 1051 (2009).

[9] H. Rauch, W. Treimer, and U. Bonse, Test of a single crystal neutron interferometer, Phys. Lett. A **47**, 369 (1974).

[10] L. Yuan, J. Yang, Z. Liu, and J. Sun, In-fiber integrated Michelson interferometer, Opt. Lett. **31**, 2692 (2006).

[11] A. Psarouli, A. Salapatas, A. Botsialas, P. S. Petrou, I. Raptis, E. Makarona, G. Jobst, K. Tukkiniemi, M. Sopanen, R. Stoffer, S. E. Kakabakos, and K. Misiakos, Monolithically integrated broad-band mach-zehnder interferometers for highly sensitive label-free detection of biomolecules through dual polarization optics, Sci. Rep. **5**, 17600 (2015).

[12] C. Sturm, D. Tanese, H. S. Nguyen, H. Flayac, E. Galopin, A. Lematre, I. Sagnes, D. Solnyshkov, A. Amo, G. Malpuech, and J. Bloch, All-optical phase modulation in a cavity-polariton Mach–Zehnder interferometer, Nat. Commun. **5**, 3278 (2014).

[13] H. G. Winful, Energy storage in superluminal barrier tunneling: Origin of the "Hartman effect," Opt. Express **10**, 1491 (2002).

[14] M. Neugebauer, P. Banzer, and S. Nechayev, Emission of circularly polarized light by a linear dipole, Sci. Adv. **5**, eaav7588 (2019).

[15] D. Dai, Silicon polarization beam splitter based on an asymmetrical evanescent coupling system with three optical waveguides, J. Lightwave Technol. **30**, 3281 (2012).

[16] A. Enders and G. Nimtz, Evanescent-mode propagation and quantum tunneling, Phys. Rev. E **48**, 632 (1993).

[17] R. M. A. Azzam and A. De, Circular polarization beam splitter that uses frustrated total internal reflection by an embedded symmetric achiral multilayer coating, Opt. Lett. **28**, 355 (2003).

[18] S. Longhi, Resonant tunneling in frustrated total internal reflection, Opt. Lett. **30**, 2781 (2005).

[19] T. Q. Tran, S. Lee, H. Heo, and S. Kim, Tunable wide-angle tunneling in graphene-assisted frustrated total internal reflection, Sci. Rep. **6**, 19975 (2016).

[20] T. E. Hartman, Tunneling of a wave packet, J. Appl. Phys. **33**, 3427 (1962).

[21] J. C. Martinez and E. Polatdemir, Origin of the Hartman effect, Phys. Lett. A **351**, 31 (2006).

[22] H.-Y. Yao, N.-C. Chen, T.-H. Chang, and H. G. Winful, Frequency-dependent cavity lifetime and apparent superluminality in Fabry-Pérot-like interferometers, Phys. Rev. A **86**, 053832 (2012).

[23] J. W. Kłos, Y. S. Dadoenkova, J. Rychły, N. N. Dadoenkova, I. L. Lyubchanskii, and J. Barnaś, Hartman effect for spin waves in exchange regime, Sci. Rep. **8**, 17944 (2018).

[24] A. M. Steinberg, P. G. Kwiat, and R. Y. Chiao, Measurement of the Single-Photon Tunneling Time, Phys. Rev. Lett. **71**, 708 (1993).

[25] G. M. Gehring, A. C. Liapis, and R. W. Boyd, Tunneling delays in frustrated total internal reflection, Phys. Rev. A **85**, 032122 (2012).

[26] L. Ragni, Group delay of evanescent signals in a waveguide with barrier, Phys. Rev. E **79**, 046609 (2009).

[27] P. Eckle, A. N. Pfeiffer, C. Cirelli, A. Staudte, R. Dorner, H. G. Muller, M. Buttiker, and U. Keller, Attosecond ionization and tunneling delay time measurements in helium, Science **322**, 1525 (2008).

[28] S. Longhi, M. Marano, P. Laporta, and M. Belmonte, Superluminal optical pulse propagation at 1.5 μm in periodic fiber Bragg gratings, Phys. Rev. E **64**, 055602(R) (2001).

[29] Ch. Spielmann, R. Szipöcs, A. Stingl, and F. Krausz, Tunneling of Optical Pulses through Photonic Band Gaps, Phys. Rev. Lett. **73**, 2308 (1994).

[30] A. Fortun, C. Cabrera-Gutiérrez, G. Condon, E. Michon, J. Billy, and D. Guéry-Odelin, Direct Tunneling Delay Time Measurement in an Optical Lattice, Phys. Rev. Lett. **117**, 010401 (2016).

[31] R. Ramos, D. Spierings, I. Racicot, and A. M. Steinberg, Measurement of the time spent by a tunnelling atom within the barrier region, Nature (London) **583**, 529 (2020).

[32] A. F. Oskooi, D. Roundy, M. Ibanescu, P. Bermel, J. D. Joannopoulos, and S. G. Johnson, Meep: A flexible free-software package for electromagnetic simulations by the FDTD method, Comput. Phys. Commun. **181**, 687 (2010).

[33] K. Fasihi and S. Mohammadnejad, Orthogonal hybrid waveguides: an approach to low crosstalk and wideband photonic crystal intersections design, J. Lightwave Technol. **27**, 799 (2009).

[34] A. Shinya, S. Mitsugi, E. Kuramochi, and M. Notomi, Ultrasmall multi-port channel drop filter in two-dimensional photonic crystal on silicon-on-insulator substrate, Opt. Express **14**, 12394 (2006).

[35] S. Ogawa, M. Imada, S. Yoshimoto, M. Okano, and S. Noda, Control of light emission by 3d photonic crystals, Science **305**, 227 (2004).

[36] S.-G. Lee, S.-Y. Jung, J. Lee, J.-M. Park, and C.-S. Kee, Self-collimation-based photonic crystal Mach–Zehnder demultiplexer, J. Opt. **18**, 095103 (2016).

[37] S.-G. Lee, J.-M. Park, C.-S. Kee, and J. Lee, Self-collimation-based photonic crystal Mach–Zehnder add-drop filters, J. Phys. D **49**, 055101 (2016).

[38] G. Kaur and H. Wanare, Controlling spatial mode superposition to channel light flow in a photonic crystal, J. Opt. Soc. Am. B **37**, 3809 (2020).

[39] L. Nanda, A. Basu, and S. A. Ramakrishna, Delay times and detector times for optical pulses traversing plasmas and negative refractive media, Phys. Rev. E **74**, 036601 (2006).

[40] V. R. Bhardwaj, E. Simova, P. P. Rajeev, C. Hnatovsky, R. S. Taylor, D. M. Rayner, and P. B. Corkum, Optically Produced Arrays of Planar Nanostructures inside Fused Silica, Phys. Rev. Lett. **96**, 057404 (2006).